Preflight Radiometric Calibration of Orbiting Carbon Observatory 2

Robert Rosenberg, Stephen Maxwell, B. Carol Johnson, Lars Chapsky, Richard A. M. Lee, and Randy Pollock

***Abstract*— The imaging spectrometers of the second orbiting carbon observatory were radiometrically calibrated before launch during instrumentlevel ground testing. The gain and dark responses were characterized for each focal plane array detector element. An integrating sphere source with an integrated monitoring spectroradiometer illuminated the OCO-2 spectrometers at many light levels. Instrument output was compared with the calibrated output of the source to derive gain coefficients. This source was calibrated in situ with respect to the National Institute of Standards and Technology reference standards, and the instrument met its absolute performance requirement of 5%. Matching fields of view for the internal monitor detectors and the external instrument under test was found to be particularly important, as observed in the results and supported by modeling. Temperature-dependent dark offsets were corrected in a separate process. Solar spectra with varying neutral density filters were used to validate the linearity of the spectrometers.**

***Index Terms*— Integrating sphere, Orbiting Carbon Observatory (OCO-2), radiometry, remote sensing.**

I. Introduction

THE Orbiting Carbon Observatory 2 (OCO-2) is a National Aeronautics and Space Administration (NASA) mission designed to measure global CO_2 concentrations (XCO_2) with sufficient precision and accuracy to detect regional sources and sinks [1]. The original OCO-2 launched on February 24, 2009 but did not achieve orbit due to launch vehicle failure [2]. The follow-on mission, OCO-2, launched successfully from Vandenberg Air Force Base in California on July 2, 2014. It is in a sun-synchronous polar orbit with a 98.8-min period, and repeats its ground track every 16 days. The instrument is a nearly identical copy of the original OCO-2 instrument, and the coefficients to describe gain and noise are expressed in the same format [3], [4].

This paper addresses the preflight radiometric calibration of the OCO-2 instrument. All requirements for radiometric performance are driven by the mission objective to retrieve XCO_2 with 0.25% precision. The absolute radiometric uncertainty requirement for OCO-2 is $\leq$5% ($k = 1$; standard uncertainty) [5]. The k parameter is a coverage factor and follows international recommendations on evaluating and expressing measurement uncertainty [6]. In addition to the absolute performance requirements, linearity requirements were derived from a test where a metal screen blocked a diffuse solar beam directed into the instrument. Since the reduction in radiance should be equal for all colors, the slope of ratio versus intensity must be <0.5% and values must be consistent to $\pm$0.25% ($k = 1$). Meeting this requirement also validates the radiometric calibration process as a whole. The spectral characterization and calibration of the instrument are described in a companion paper [7]. Retrievals performed on uplooking solar spectra [8] validated the end-to-end performance of the instrument and calibration coefficients.

Section II gives an overview of the instrument and the data it acquires. Section III describes the calibration chain, the measurement apparatus, and the procedures followed by the National Institute of Standards and Technology (NIST) and the Jet Propulsion Laboratory (JPL), California Institute of Technology to establish the calibration and validate the linearity. Sections IV and V review the data acquired during calibration, addressing and tabulating uncertainties and systematic effects. Section VI addresses the characterization of residual image, which was a significant issue on OCO-2 but is of minimal importance on OCO-2. Finally, Section VII summarizes the results with an emphasis on lessons learned.

II. Instrument Overview

The OCO-2 instrument measures sunlight reflected by Earth's surface and atmosphere in three narrow spectral channels. The spectral ranges include regions with strong absorption by CO_2 and O_2 as well as regions with little to no absorption of sunlight by atmospheric gases. These continuum regions help to constrain the effects of variations in surface albedo and aerosols [1]. Spectra collected by OCO-2 during ground testing at JPL, showing atmospheric absorption imprinted on the solar spectrum, are shown in Fig. 1.

The instrument incorporates three high-spectral resolution imaging, grating spectrometers that share a common telescope [9]. A schematic of the instrument, including the layout of three spectrometers and associated detectors, is shown in Fig. 2. Table I contains the spectral band designations used throughout this paper, along with the primary absorbing gas, spectral range, spectral resolution, dynamic range, and typical signal-to-noise ratio for each channel. The diffraction gratings within each spectrometer transmit one polarization far more efficiently than the other. To reduce stray light, a linear polarizer was installed in front of the spectrometer slit to reject light with the polarization that is mostly reflected by the grating. The orientation of the polarizers was

Manuscript received January 5, 2016; revised August 23, 2016 and October 20, 2016; accepted November 23, 2016. This work was supported by the Jet Propulsion Laboratory, California Institute of Technology through the National Aeronautics and Space Administration.

R. Rosenberg, L. Chapsky, R. A. M. Lee, and R. Pollock are with the Jet Propulsion Laboratory, California Institute of Technology, Pasadena, CA 91109-8099 USA (e-mail: Rob.Rosenberg@jpl.nasa.gov).

S. Maxwell and B. C. Johnson are with the National Institute of Standards and Technology, Gaithersburg, MD 20899 USA.

Color versions of one or more of the figures in this paper are available online at http://ieeexplore.ieee.org.

Digital Object Identifier 10.1109/TGRS.2016.2634023

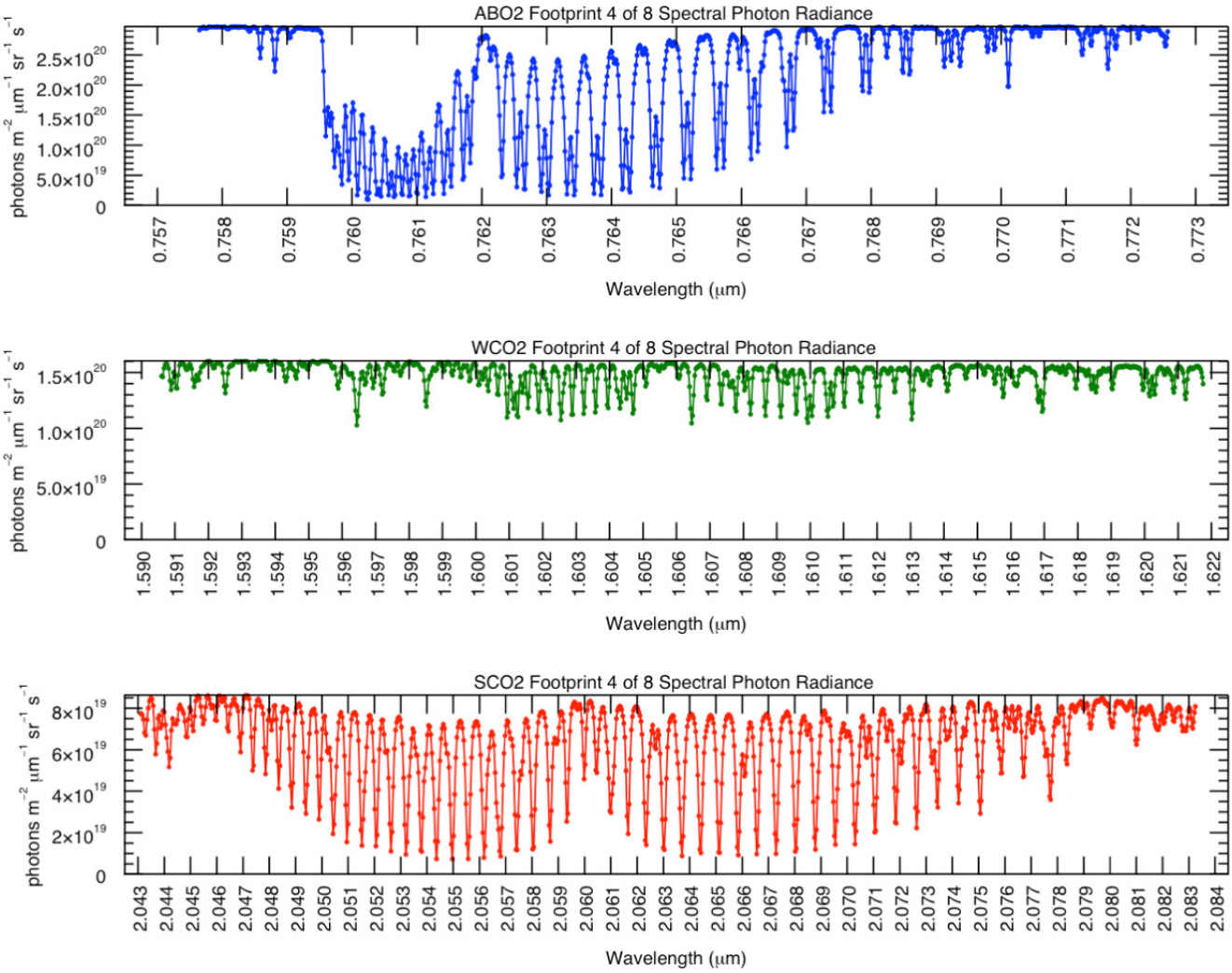

Fig. 1. Spectra from ground testing in April 2012 show that the instrument can resolve the narrow absorption features in all three bands. These measurements were acquired with an unblocked heliostat beam with the sun 67.3° above the horizon.

chosen to maximize the throughput through the polarizer-grating system. It was incorrectly assumed during instrument design that these components selected the polarization parallel to the entrance slit. Inflight data showed that it actually maximized the throughput polarized perpendicular to the slit. Changes were made to both the operational observing geometry and data analysis to recover signal-to-noise and maintain XCO_2 accuracy. This error does not affect the preflight calibration testing and radiometric accuracy calculations reported in this paper, because the integrating sphere source (ISS) is unpolarized.

At each spectrometer's focus, a 1024 × 1024 focal plane array (FPA) records the spectrum in one dimension (columns), while the spatial dimension (rows) measures field angles along the slit. All detectors are Hawaii-1RG manufactured by Teledyne Scientific and Imaging, LLC,[1] with operating temperatures near 120 K to minimize dark current and, in the case of the ABO2 channel, residual image (see Section VI). The ABO2 detector is silicon; the WCO2 and SCO2 detectors are HgCdTe. The instrument digitizes 220 rows but only about 160 rows are used to create science data products. In the spectral dimension, four pixels on each end of the FPA are masked, leaving 1016 spectral samples per footprint. Approximately 1% of the pixels in the science area was identified as "bad pixels" during prelaunch testing and their data are not used.

The 160 rows used for science data products are averaged in eight groups of 20 pixels per column to reduce data volume. This yields eight independent spatial footprints, each with an along-slit field of view of 0.1° (about 1.3 km wide when viewing at nadir with the spectrometer slit oriented perpendicular to the ground track). Each FPA is read out using a rolling readout with a 3-Hz frame rate, and time-averaged surface footprints on the ground are shaped like parallelograms. The length defined by the spacecraft motion during each exposure is approximately 2.3 km. Since the OCO-2 spacecraft rotates almost 180° around the telescope's optical axis once each orbit to maintain polarization sampling relative to the solar

[1]Certain commercial equipment, instruments, or materials are identified in this paper to foster understanding. Such identification does not imply recommendation or endorsement by NIST, nor does it imply that the materials or equipment identified are necessarily the best available for the purpose.

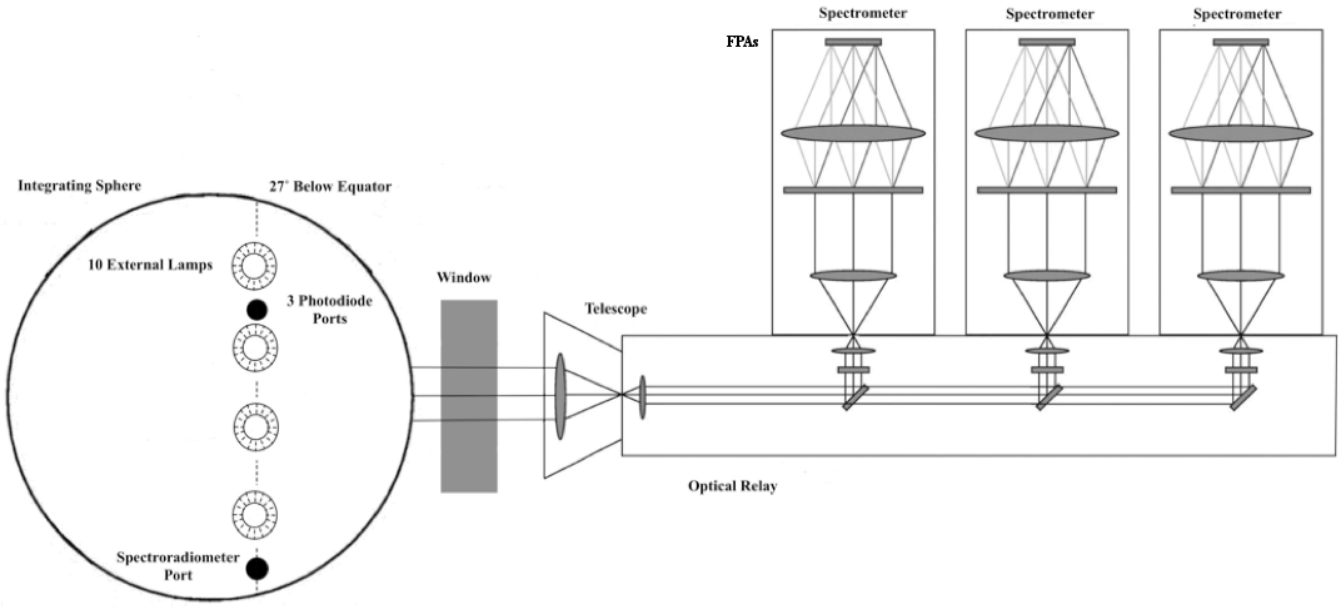

Fig. 2. Schematic of the integrating sphere, window, and OCO-2's three spectrometers. The lamps are oriented normal to the sphere surface, while mounts of the spectroradiometer and photodiodes are pointed toward the top.

TABLE I
SPECTRAL BANDS MEASURED BY OCO-2

Band Designation	Absorbing Gas	Spectral Range (nm)	Spectral Range (cm^{-1})	Typical Spectral Resolution ($\lambda/\Delta\lambda$)	Dynamic Range (photons m^{-2} μm^{-1} sr^{-1} s^{-1})	SNR for 5 % Albedo & 60° SZA
Oxygen A-Band (ABO2)	O_2	757.6 to 772.6	12943 to 13120	18500	7.50×10^{16} to 7.00×10^{20}	263
Weak Carbon Dioxide (WCO2)	CO_2	1590.6 to 1621.8	6166 to 6287	19200	2.15×10^{16} to 2.45×10^{20}	358
Strong Carbon Dioxide (SCO2)	CO_2	2043.1 to 2083.4	4800 to 4895	19800	2.15×10^{16} to 1.25×10^{20}	285

Note that the dynamic range uses radiance for the component of light with its polarization aligned with the instrument's response. The equivalent radiance of an unpolarized scene is twice these values.

azimuth [1], the widths of the footprints vary continuously along the orbit track. The footprint area on the ground thus varies from about 3 km^2 to less than 1 km^2 as a function of latitude and season. Note that the instantaneous field of view remains constant and therefore changing footprint size does not alter radiance sensitivity.

The calibration is required to be valid over a broad range of radiance levels to accommodate variations in solar illumination, surface and atmospheric reflectance, as well the large contrasts between gas absorption line cores and the adjacent continuum, whose positions on the FPA change due to Doppler shifts. The OCO-2 SCO2 maximum signal requirement was increased by 50% from the value selected for OCO-2 based on statistics derived from measurements by the Greenhouse gases Observing SATellite (GOSAT) satellite [10]. GOSAT is a joint project of the Japan Aerospace Exploration Agency, the Ministry of the Environment, and the National Institute for Environmental Studies, and has been in operation since 2009. The OCO-2 instrument samples subsets of the same spectral regions measured by the GOSAT thermal and near-infrared sensor for carbon observation Fourier transform spectrometer.

The instrument noise level of OCO-2 was characterized in an identical manner as OCO-2 [3]. Two coefficients are calculated for every spectral sample, a constant "background" term and a "photon" shot noise term proportional to the square root of radiance. In (1) and (2), radiances are expressed as percentages of $N_{\max}$, the maximum measureable signal specification from Table I. Also listed in Table I is typical signal-to-noise ratios from the same theoretical illumination level considered for OCO-2: a 5% albedo surface viewed at a solar zenith angle of 60°

$$\sigma_N = \frac{N_{\max}}{100}\sqrt{\left|\frac{100N}{N_{\max}}\right| c^2_{\text{photon}} + c^2_{\text{background}}} \tag{1}$$

$$\text{SNR} = \frac{N}{\sigma_N} = \sqrt{\frac{100N^2}{N_{\max}\left(c^2_{\text{background}}\frac{N_{\max}}{100} + c^2_{\text{photon}}N\right)}}. \tag{2}$$

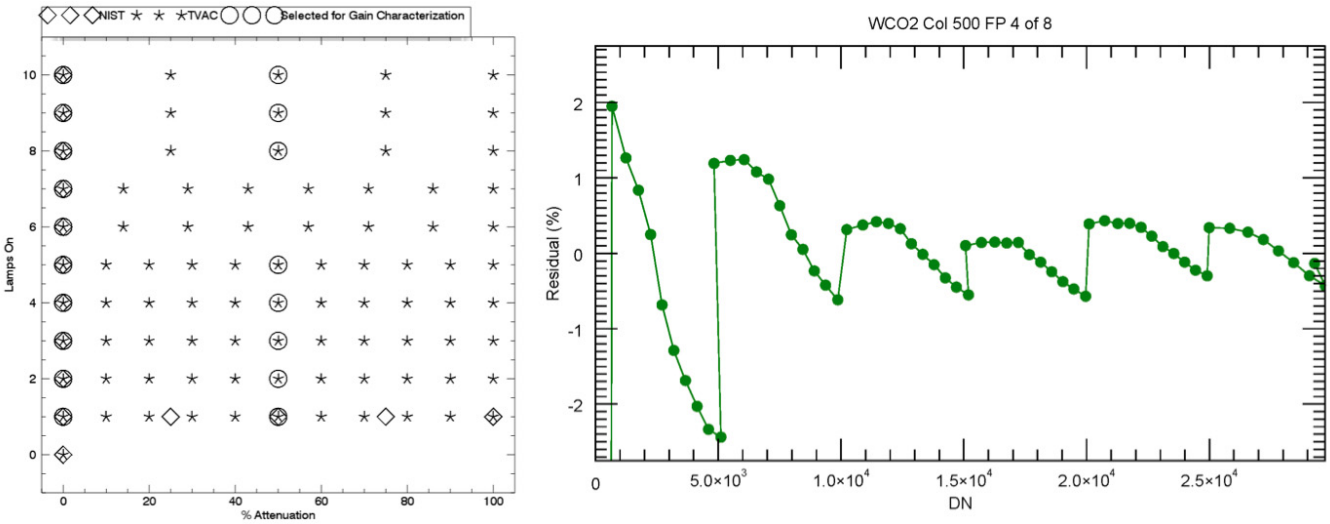

Fig. 3. (Left) Most sphere configurations acquired during JPL testing were not measured with the NIST Analytical Spectral Devices (ASD). Only the ten measurements without Lamp 8 attenuation and the eight levels with the variable attenuator at 50% remained. (Right) Fractional radiance residuals when all sphere configurations used the same ASD calibration.

III. Calibration Procedure

A. Radiometric Gain Calibration

All OCO-2 prelaunch radiometric calibration measurements were performed while the instrument was installed in a 3 m diameter thermal-vacuum (TVAC) chamber at NASA JPL that simulates the on-orbit environment. The instrument was installed such that the telescope aperture viewed upward in the zenith direction through a fused silica window. The sources and standards used in the radiometric calibration tests were installed on a deck above the TVAC chamber. The primary stimulus used for absolute radiometric calibration was a 1 m diameter, barium sulfate coated ISS that was positioned over the window such that it illuminated OCO-2 instrument in the nadir direction. In addition to the radiometric calibration, spectral, spatial, and polarimetric properties of the instrument were characterized during these tests, along with linearity tests based on neutral density screens described in Section III-C. Different properties of the OCO-2 instrument were characterized during four tests from October 2011 to April 2012 with a total duration of approximately ten weeks. The final radiometric calibration was determined by measurements in the final test cycle, expanded in more detail in Table II.

The ISS, manufactured by Labsphere, Inc., is equipped with ten lamps external to the sphere. These lamps are evenly spaced along a circle at a polar angle of 27° below the equator of the sphere (63° above the point centered on the sphere exit aperture). Lamp 8 is behind a variable attenuator, an opaque metal sheet driven by an actuator that obscures the lamp entrance hole. The combination of active lamps and the position of the variable attenuator define the configurations c that are shown in Fig. 3, yielding the different radiance levels $L_{\mathrm{ISS}}(c, \lambda_j)$. During a single calibration run, 85 levels interspersed with 12 zero radiance measurements (to measure $dN_{j,\mathrm{dark}}$) were used to characterize the OCO-2 instrument. Lamps are turned OFF in the following order: 1, 4, 7, 10, 3, 6, 9, 2, and 5. This was done to maximize spatial uniformity of the illumination and to have Lamp 8, which is attenuated, ON at all times.

TABLE II
Listing of Measurement Activities

Location	Dates	Activity	Symbol
JPL	22 to 25 Jan 2012	Initial Characterization	t_0
NIST	28 Feb 2012	Calibration of ASD2 with NPR	t_1
JPL	6 to 8 Mar 2012	NIST Measurements of JPL ISS	t_2
NIST	15 Mar 2012	Calibration of ASD2 with NPR	t_3
NIST	18 Mar 2012	Calibration of NPR at FASCAL	t_4
JPL	12 to 23 Apr 2012	Calibration of OCO-2 with ISS	t_5

The spectrum of the light emitted into the integrating sphere is determined by interference filters placed between each lamp and its entrance port. These filters simulate the relative spectral radiance of a 5800 K blackbody in the three bands of interest. Without them, the spectrum would have been that of a 2800 K blackbody, and the ratio of SCO2 to ABO2 radiance would have been too high. An artifact of these filters is that the sphere outputs a salmon color as shown in Fig. 4. The radiance of the ISS is monitored by four fiber-coupled radiometers; three are filter radiometers with narrow-band spectral filters centered on the OCO-2 bands and the fourth is a commercial spectroradiometer, an ASD FieldSpec3[2] (referred to as the "JPL ASD" or just "ASD"). These sensors are placed in the

[2]PANalytical B.V., Boulder, CO, USA.

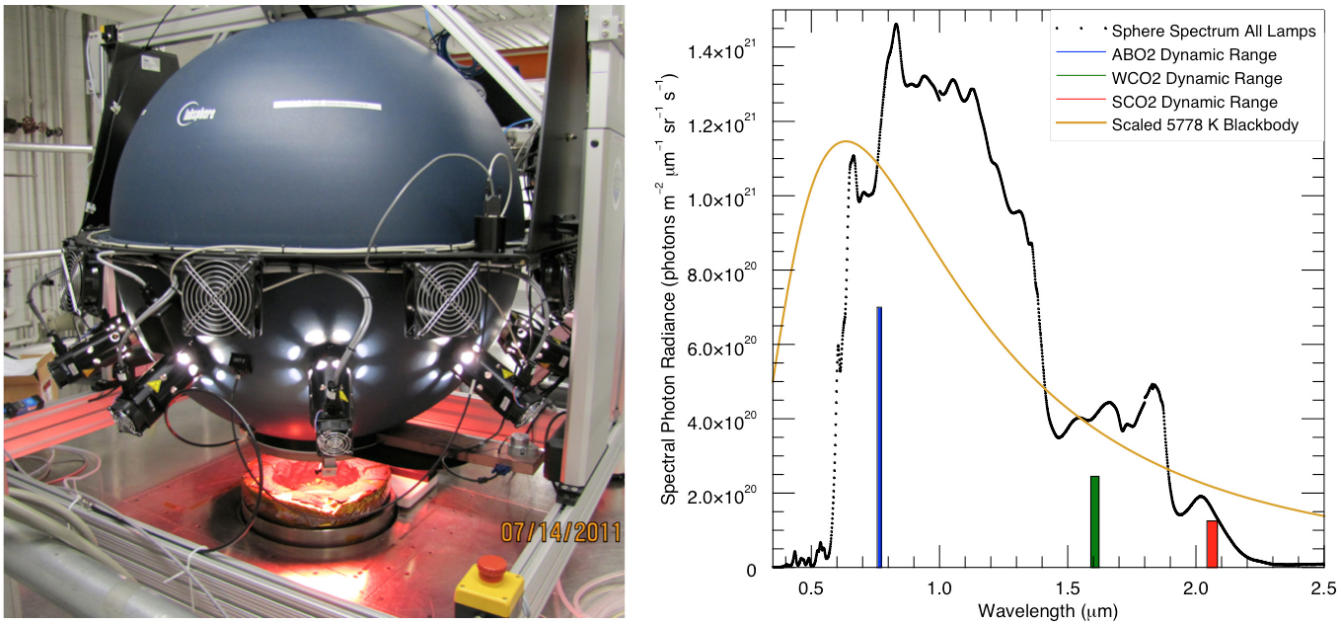

Fig. 4. (Left) Salmon colored light is the result of filters over the white lamps that tailor the spectrum to appear closer to a solar blackbody at the three narrow OCO-2 bands. (Right) Output spectrum of the sphere with the OCO-2 dynamic range requirements and bands overlaid.

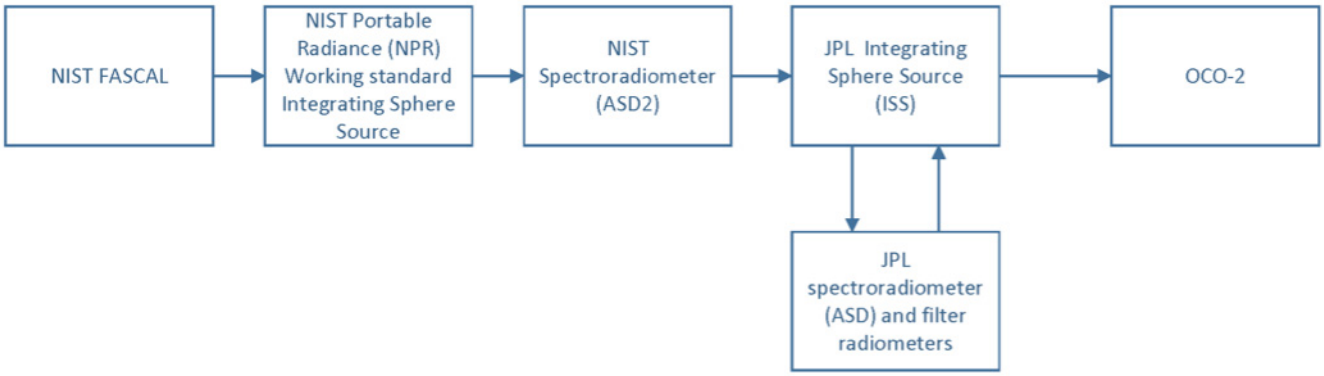

Fig. 5. Illustration of the OCO-2 calibration chain. NIST provided an *in situ* calibration of the JPL ISS and ASD at a set of lamp configurations. The ISS presented a set of levels to OCO-2, and the radiances used during this calibration were determined by the concurrent readings of the ASD.

same plane as the lamps but are mounted such that their fields of view are at the top of the sphere. The ASD field of view is approximately 25° in the ABO2 band.

In this paper, the radiometric calibration of the OCO-2 instrument was made traceable to the NIST Facility for Automated Spectroradiometric Calibrations (FASCAL) through the JPL ISS and its internal JPL ASD spectroradiometer, an NIST spectral radiance reference standard ISS (the NIST Portable Radiance (NPR) source), and an NIST ASD transfer spectroradiometer, termed the ASD2 in this paper. The OCO-2 instrument was calibrated using the JPL ISS at a set of predefined configurations that provide different radiance levels. The spectral radiance of the JPL ISS was determined using the spectral flux responsivity values of the JPL ASD, which had been assigned using the ASD2. The ASD2 was calibrated for spectral radiance responsivity using the NPR, and the NPR calibrated for spectral radiance using FASCAL. The full calibration chain is shown in Fig. 5.

As a result of these steps, which included measurements with the shutter of the JPL ISS closed, OCO-2 response to illumination is expressed using a set of temperature-dependent dark offsets (described in Section III-B) and a set of gain coefficients ($g_{i,j}$) for a polynomial that relates instrument readout in digital numbers (DN_j) to radiance for each spectral sample j of the detector. The gain coefficients are derived for each spatial footprint (index omitted) from a fit to the polynomial equation with summation index i

$$L_{\mathrm{ISS}}(c, \lambda_j) = \sum_{i=1}^{5} g_{i,j}(DN_j(c) - DN_{j,\mathrm{dark}})^i \qquad (3)$$

where $L_{\mathrm{ISS}}(c, \lambda_j)$ is the calibrated radiance of the JPL ISS for a given configuration c, at the wavelength λ_j, $DN_j(c)$ is the OCO-2 instrument readout for that sphere configuration, and $DN_{j,\mathrm{dark}}$ is the temperature corrected dark offset. The wavelengths λ_j are obtained from a separate set of tests that determines the spectral calibration of the instrument.

The spectral flux responsivity of the JPL ASD spectroradiometer, as determined using the NPR and the ASD2, is taken to be stable from t_2 to t_5 (see Table II), and therefore,

the spectral radiance scale of the JPL ISS is referenced to the JPL ASD for the OCO-2 calibration via the equation

$$L_{\mathrm{ISS}}(c, \lambda_j) = DN^{\mathrm{ASD}}_{j,\mathrm{ISS}} \cdot k^{\mathrm{ASD}}_j(c) \tag{4}$$

for example, during the calibration of OCO-2, the ASD digital readout ($DN^{\mathrm{ASD}}_{j,\mathrm{ISS}}$) is used to determine the spectral radiance $L_{\mathrm{ISS}}(c, \lambda_j)$. The different field of view of the ASD requires that a different set of calibration coefficients $k^{\mathrm{ASD}}_j(c)$ be derived for each configuration of the lamps illuminating the ISS. The combinations of powered lamps and attenuator position are shown in Fig. 5. The filter radiometers served to validate changes in output observed by the ASD, but were not used directly in any calculations. The ASD reports spectral radiance with a resolution of 3 nm and a sampling of 1.4 nm in the ABO2, and a resolution of 10 nm and a sampling of 2 nm in the WCO2 and SCO2 bands. The OCO-2 detectors sample the incident radiation at a resolution of tens of picometers, so assigning a radiance value to each OCO-2 sample requires interpolating the ASD spectrum. This is done with a linear fit to the reported ASD spectral radiances. In contrast to the 1016 spectral samples in each OCO-2 band, the ASD provides 17, 33, and 42 samples for the ABO2, WCO2, and SCO2 bands, respectively.

The calibration of the ASD and, therefore, the ISS was performed by NIST and JPL in two sets of joint tests at JPL, the second of which resulted in the calibration that was ultimately used. In these calibrations, the ASD2 performed simultaneous measurements of the JPL ISS with the ASD. Along with the radiance measurements, a set of ISS operational data, including lamp voltages and currents, was recorded. The ASD2 uses a 1° field of view foreoptic pointed at zenith and was mounted inside the TVAC chamber (then operating at room temperature and atmospheric pressure) where it viewed the sphere through the fused silica window. The 1° foreoptic was chosen because it was used for the measurements made initially at NIST. For these JPL measurements, it would have been better to choose a foreoptic that matched the larger field of view of OCO-2, determined primarily by the size of the telescope aperture. Viewing the ISS through the chamber window in the same configuration used for the subsequent calibration of the OCO-2 instrument avoided the need to correct for the window's transmittance or back reflections into the ISS. The calibration coefficients for the ASD are then derived from

$$k^{\mathrm{ASD}}_j(c) = \frac{DN^{\mathrm{ASD2}}_{j,\mathrm{ISS}}(c)}{DN^{\mathrm{ASD}}_{j,\mathrm{ISS}}(c)} k^{\mathrm{ASD2}}_j \tag{5}$$

where $k^{\mathrm{ASD2}}_j$are the calibration coefficients of the ASD2 and$DN^{\mathrm{ASD}}_{j,\mathrm{ISS}}(c)$ and $DN^{\mathrm{ASD2}}_{j,\mathrm{ISS}}(c)$ are the digital readouts of the ASD and ASD2 when observing ISS configuration c.

The calibration coefficients of the ASD2 were derived from repeated viewing of the NPR at a single radiance level [11]. NPR is a well-characterized broadband ISS with four internal 30-W unfiltered quartz tungsten halogen lamps and two internal filtered detectors. The calibration equation for a single viewing of NPR at each wavelength is $L_{\mathrm{NPR}} = DN^{\mathrm{ASD2}}_{\mathrm{NPR}} \cdot k^{\mathrm{ASD2}}$. These FASCAL data are interpolated from the provided 10-nm grid to the 1-nm grid reported by the ASD2 using smoothing splines for ABO2 and WCO2 and the second-order local polynomial regression for SCO2. In addition, within the ABO2 band, the path length of light in the NPR sphere was estimated and an about 0.5% correction was made to account for O_2 absorption, based on a simulated absorption spectrum generated using the HIgh-resolution TRANsmission molecular absorption database database [12]. The uncertainty introduced in these steps is insignificant, although it is important to note that interpolation introduces highly correlated uncertainties between adjacent wavelengths. Therefore, band averages have no less uncertainty than the individually reported wavelengths. The calibration coefficients used are the average of those derived from viewing NPR before and after the JPL deployment.

Combining all the steps and making the date of the measurement explicit yields the measurement equation

$$L_{\mathrm{ISS}}(t_5, c) = DN^{\mathrm{ASD}}_{\mathrm{ISS}}(t_5, c) \cdot \frac{DN^{\mathrm{ASD2}}_{\mathrm{ISS}}(t_2, c)}{DN^{\mathrm{ASD}}_{\mathrm{ISS}}(t_2, c)} \cdot \frac{2L_{\mathrm{NPR}}(t_4)}{\left(DN^{\mathrm{ASD2}}_{\mathrm{NPR}}(t_1) + DN^{\mathrm{ASD2}}_{\mathrm{NPR}}(t_3)\right)} \tag{6}$$

with the dates t listed in Table II. The term containing the NPR radiance is the calibration coefficient of the ASD2.

To complete the required measurements in the time available and allow repeat measurements, the *in situ* NIST calibrations only used the JPL ISS in 13 different configurations: leaving the variable attenuator fully open as the first nine lamps turned OFF, then blocking 25%, 50%, and 75% of the final lamp. In contrast, the TVAC test procedure illuminated the instrument with 85 different sphere configurations, most of which could not be used in this analysis, because they did not correspond to a configuration measured directly by NIST. Only data collected with the variable attenuator open and at 50% were used, but these 18 remaining configurations provided sufficient information to constrain the polynomial fits. For the eight light levels where the variable attenuator was 50% open, radiances were not calculated by directly using (6), but rather by linearly combining radiances from only Lamp 8 at 50% and the appropriate number of lamps with no attenuation. The selected configurations are shown in Fig. 3, along with curve fitting residuals from an attempt to derive gain coefficients using the full ensemble of sphere configurations. This supports the decision to calibrate the ISS and ASD at each configuration, as the saw-tooth-like structure reflects the variable attenuator position and which lamps were ON inside the sphere. This issue, also identified during OCO-2 calibration [3], is due to the combination of nonuniform illumination and the monitor spectroradiometer viewing a larger region of the ISS compared with OCO-2.

OCO-2 readout noise is incorporated into the gain calculations, but was reduced to a negligible level by acquiring 900 frames per sphere configuration. Note that during flight, this measurement noise will play a larger role because each frame will have a unique illumination pattern, but is still well within specifications. Finally, it should be noted that for each sample, all configurations that produced a saturating light level were excluded.

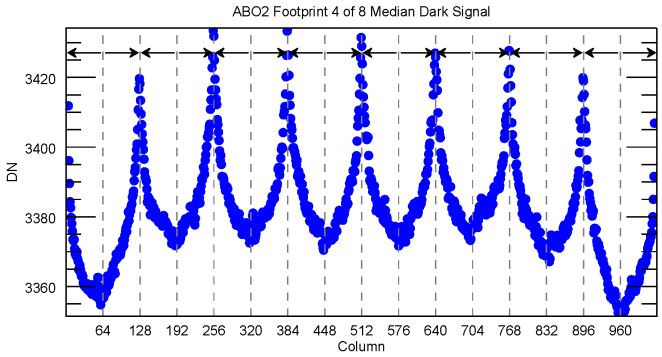

Fig. 6. Example of the fixed "W" pattern for a single footprint of the ABO2 detector. Vertical dashed lines indicate the locations of the readout taps, and arrows indicate the read direction.

B. Dark Offset Correction

As described earlier, the dark offset $DN_{j,\text{dark}}$ was measured during radiometric calibration and other test procedures. These offsets, if uncorrected, would manifest as a linearity bias and directly affect OCO-2 atmospheric retrievals. The dominant feature of the dark offset is a fixed "W"-shaped pattern aligned with the locations of the 16 taps of the readout multiplexer, which each read 64 columns of the detector (Fig. 6). Smaller scale patterns, including variations in shape of this "W" pattern, persist as well. The values of $DN_{j,\text{dark}}$ varied beyond the level of readout noise, and this variation was well correlated with temperatures of different OCO-2 instrument components.

To correct this variability in $DN_{j,\text{dark}}$, fits were made to an equation of the form

$$DN_{j,\text{dark,corrected}}(T_1, T_2) = DN_{j,\text{dark}}\left(T_1^*, T_2^*\right) - k_1 \cdot \left(T_1 - T_1^*\right) - k_2 \cdot \left(T_2 - T_2^*\right) \quad (7)$$

where T_1 is the FPA temperature and T_2 is the optical bench temperature. The $*$ indicates a reference value, chosen as a weighted average of 25 measurements. The locations of these two temperatures, also chosen for OCO-2 [3], were selected due to physical intuition, but were later confirmed to explain the maximum amount of variance out of 34 of temperatures that were measured. The sensitivity to detector temperature is expected based on device physics, and the sensitivity to optical bench temperature arises from the blackbody radiation from these components.

C. Linearity Tests

To test the linearity of the detectors, the signal ratio test developed for OCO-2 [3] was performed for OCO-2. In this ground-based test, a heliostat directs sunlight onto a Spectralon[3] panel, with additional mirrors directing diffuse sunlight into the OCO-2 telescope. The atmosphere between the sun and the instrument introduces a pattern of spectral features caused by absorbing O_2 and CO_2 [8]. The maximum depth of this absorption relative to the continuum is approximately 95%, 37%, and 91% for the ABO2, WCO2, and SCO2, respectively. Next, four metal screens with regularly spaced holes are inserted (one at a time) between the heliostat and the Spectralon panel to reduce illumination at all wavelengths by approximately 75%, 50%, 25%, and 10%. The feature size of the screens is such that diffraction effects should not introduce significant spectral dependence. Linearity is evaluated by comparing the calibrated radiances reported by the instrument across all wavelengths in each channel; the ratios of the reduced to the unreduced radiances should be independent of wavelength and radiance. A change in optical path length or atmospheric conditions during the test could introduce wavelength-dependent changes in radiance. To minimize errors due to this effect, the test was started less than 1 h before solar noon.

IV. Results

A. Radiometric Gain Calibration

Gain coefficients $g_{i,j}$ were calculated using the calibrated radiances of the ISS and weighted fits to the polynomial equation (3) for every spectral sample of every spatial footprint of each of the three FPAs (approximately 24 000 polynomials). Fits using polynomial orders between one and five, which is the maximum degree that can be accommodated by the science data system, were investigated. Inspections of the uncertainties in the gain coefficients and the structure of the fit residuals led to the adoption of third-order polynomials for all three OCO-2 bands. This choice was confirmed by comparing polynomial fits of different orders for the gain curves of Footprint 4, Column 500 from each band using both the F-test and Akaike's Information Criterion test in the OriginPro[4] commercial software package. An example of residuals and a derived fit quality metric are shown in Fig. 7.

In the initial polynomial fits, it was observed that the estimated uncertainties in the data were small compared with the observed spread in the residuals. Based on the statistical principle that for Gaussian random noise, two thirds of the error bars of the residuals should cross zero, 0.1%, 0.3%, and 0.25% of uncertainty were added to each band (ABO2, WCO2, and SCO2, respectively) for unattributed error. Because this was a fractional uncertainty added, it directed the fit routine to add more weight to the lower light levels. While this step was motivated by intuition, it was found later to reduce the variance in the data for the linearity test, which provides an independent indication of improved fit quality.

To derive the final gain coefficients, the aggregate of five calibration runs was used (all t_5 in Table II). Histograms of the fit residuals reveal a bifurcation for all three bands (Fig. 8). Individual populations are separated by roughly 0.5%, 0.3%, and 0.3% for each band. These two groups of calibration runs were performed 10 days apart, with a thermal cycle occurring in between as well as the ISS being removed and repositioned.

Ratios of data taken from the different groups exhibit sharp spectral lines in the ABO2, but not the WCO2 or SCO2. These patterns were caused, in part, by a thin film of ice that formed on the FPA during the first two runs. This ice built up following a temporary cryocooler failure and was removed during the

[3]Labsphere, Inc., North Sutton, NH, USA.

[4]OriginLab Corporation, Northampton, MA, USA.

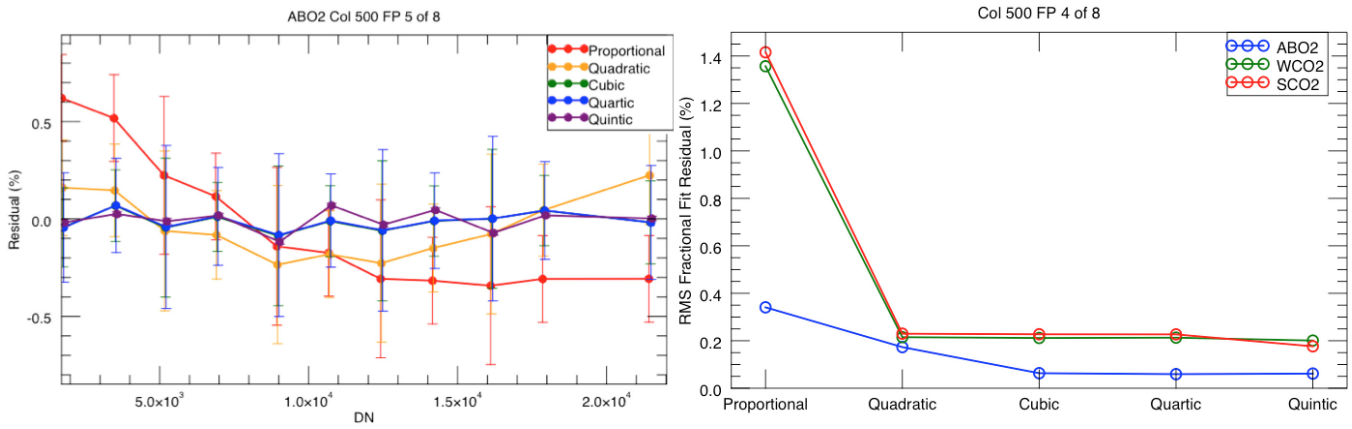

Fig. 7. (Left) Example of a single spectral sample's fit residuals for various polynomial orders. Note that the first-order fit is proportional, not linear; since dark correction is performed beforehand, the intercept at zero radiance was set to zero counts. Cubic and quartic are indistinguishable. (Right) Demonstration of the fit quality as a function of order for all three bands. The ABO2 clearly requires a cubic fit, while the WCO2 and SCO2 bands are nearly as good with a quadratic polynomial. For simplicity, a cubic was used in all three bands.

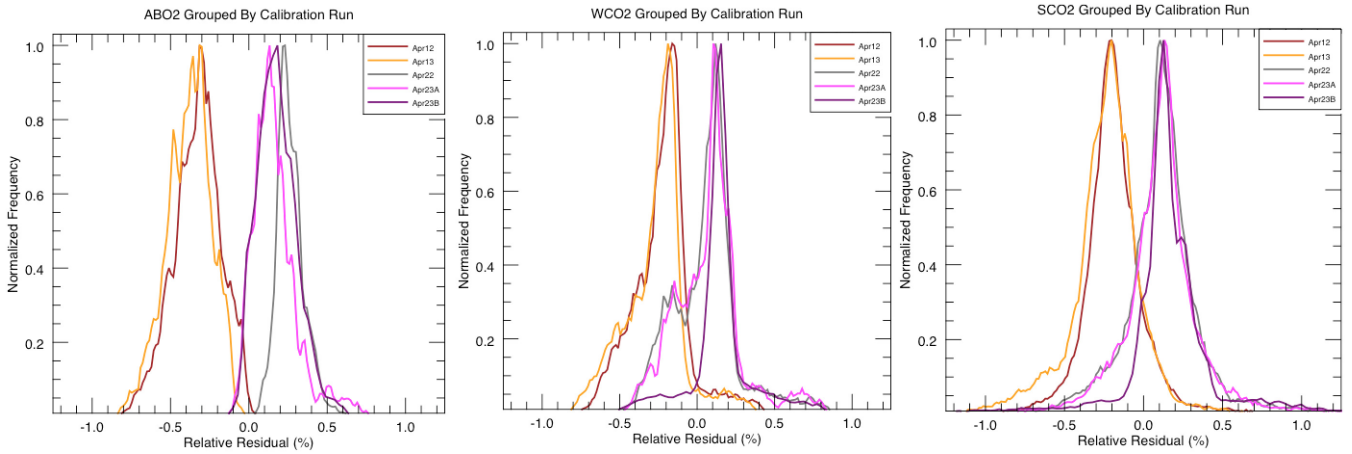

Fig. 8. Distributions of curve fitting residuals combining spectral samples and sphere configurations and separated by calibration runs. There is a clear separation between earlier and later runs. Additionally, in the WCO2 and SCO2 channels, a smaller separation exists between configurations with the variable attenuator fully open and half open. This is confirmed by the "Apr23B" run, which only included fully open configurations and exhibits a single, positive peak.

thermal cycle. The spectral and spatial patterns of the ice were most easily seen in the "single pixel" calibration mode where all 220 digitized rows are returned at a reduced frame rate.

Despite the potential perturbation of the calibration due to ice formation, it was found preferable to use all five runs rather than only the final three. The spectral features caused by the ice were very small in magnitude, at worst 0.2% on a relative basis. Also, several other attributes can also be responsible for the bifurcation: differences in the completeness of the gaseous nitrogen purge of the ISS, alignment repeatability, instrumental drift (temperature dependent or otherwise), variation in the sphere illumination pattern, and errors in estimating radiances for configurations with the attenuator at 50% that were not directly measured by NIST. The decision to average these features together was validated when substantial improvements in the signal ratio test were observed using both data groups instead of only one.

Due to the non-Gaussian distribution of the fit residuals and the finite number of calibration runs included in the fits, there is no unique choice for the method to compute uncertainty in the fit. The true uncertainty is likely bounded by two estimates: half the distance between the two peaks in the histogram of residuals, and the half-width of the window that encompasses 95% of the residuals. Because we seek to characterize each spectrometer with a single fractional uncertainty, we choose the bound that encompasses 95% of the fit residuals. This is 0.5% for the ABO2 and WCO2 and 0.6% for the SCO2. Note that this method of estimating uncertainty includes the unattributed error discussed earlier.

When analyzing long term trends, it was discovered that both the ASD and filter radiometers reported the sphere to be brighter in the CO_2 bands by as much as 2% for JPL calibration tests on t_5 compared with the NIST calibration run in March 2012. During the initial calculation of the OCO-2 gain coefficients, it was assumed that this excess light was due to retroreflection from the secondary mirror of the OCO-2 Cassegrain telescope. Based on this hypothesis, a correction was applied to account for retroreflected light that would be incident on OCO-2 but not measured by the ASD. A very small error (less than 0.2%) introduced by this correction currently exists in the OCO-2 gain coefficients. During the final analysis, it became clear that the correction factor was in error and

also that the source of the increased brightness was likely not retroreflection, as outlined in the following. Further details on how the initial correction factors were calculated are given in the Appendix.

Several explanations were sought to explain the higher brightness, including the aforementioned retroreflection from the OCO-2 collimating telescope, aging of the lamps (which tends to shift a spectrum toward the infrared), and varying power levels delivered by the power supplies to the lamps. The latter two of these explanations can be easily ruled out. Lamp aging would be monotonic, but the NIST calibration of the ISS occurred between an initial calibration run t_0 in January 2012 (not used to derive gain coefficients) and t_5 (the final calibration of OCO-2 by JPL, Table II), with higher brightness observed in both JPL data sets. The possibility of varying lamp power levels was ruled out by investigating the data acquisition files of the power supply voltages and currents. The power delivered to the lamps varied within 0.3% across all the data, with no observable correlation with the observed increase in infrared sphere radiance.

Another possible source of the higher brightness is retroreflection from the secondary mirror of the OCO-2 Cassegrain telescope. To assess this mechanism, consider the geometry of the ISS and OCO-2 system. The limiting aperture of the baffle assembly in front of the sphere, the distance from the aperture to the OCO-2 collimating telescope, and the size of that telescope put an upper limit on the retroreflection at $<0.1\%$ of the sphere output power, which means that direct retroreflection from the telescope cannot explain the increased radiance. This direct retroreflection would also not show the spectral dependence observed. Furthermore, baffles along the optical path preclude the possibility of a significant fraction of light hitting a surface other than the telescope before hitting the telescope and returning into the sphere.

To verify that a significant effect was not overlooked by these geometric considerations, NIST constructed a simplified ray trace model of the sphere and OCO-2 system. The model allowed us to rule out the possibility that reflections from baffles in front of the telescope could have retroreflected significant light and confirmed that the retroreflected power is within the bounds stated earlier. In fact, the retroreflected power that reenters the sphere in the model is approximately 0.02% of the total sphere power output, confirming that retroreflection from OCO-2 cannot be the source of the increase in radiance observed by the ASD.

However, the model did reveal an overlooked bias that affects the calibration of retroreflecting systems by integrating spheres. This bias is caused when light entering an integrating sphere encounters its first reflection from the sphere surface. This reflection is unique in that the reflected power is concentrated into a small area. Light from all subsequent reflections is, in the ideal case, uniformly distributed throughout the sphere. If the device under calibration and the sphere monitor detectors do not have a matched viewing area on the sphere surface, then large changes in radiance observed by the device under calibration may show up only as small changes in the radiance observed by the monitors, or vice versa. In the case of OCO-2, a bounding worst case was modeled where the retroreflected light would fall largely within the field of view of OCO-2 and fully outside of the field of view of the monitor spectroradiometer. This is closely related to the issue discussed earlier that results in a nonlinear relationship between sphere output and the radiance observed by the monitors.

The bias in this case can be estimated by considering the radiance observed by the monitor detectors due to the retroreflected power and the radiance observed by OCO-2 due to this power. The excess radiance is due to an increase in irradiance, which we approximate as $(\Phi_{\mathrm{br}}\rho/\pi A_{\mathrm{br}})$, where Φ_{br} is a uniform increase in photon flux, A_{br} is the area over which this flux is incident, and ρ is the sphere surface reflectivity. The manufacturer reported values of ρ are 98%, 94%, and 90% for each band. The increase in observed radiances by OCO-2 and by the monitor detectors will be

$$\Delta L_{\mathrm{OCO-2}} = \frac{\Phi_{\mathrm{br}}\rho}{\pi A_{\mathrm{br}}} + \frac{\Phi_{\mathrm{br}}}{\pi A_{\mathrm{ISS}}} \frac{\rho}{1-\rho(1-f)} \tag{8}$$

$$\Delta L_{\mathrm{MON}} = \frac{\Phi_{\mathrm{br}}}{\pi A_{\mathrm{ISS}}} \frac{\rho}{1-\rho(1-f)} \tag{9}$$

where A_{ISS} is the area of the inside of the sphere, f is the so-called "port fraction" that represents the fraction of the sphere which is open or otherwise uncoated. Using the exit port dimensions, f was calculated to be 1.3%. The bias introduced by this is then given by

$$\frac{\Delta L_{\mathrm{OCO-2}}}{\Delta L_{\mathrm{MON}}} = 1 + \frac{A_{\mathrm{ISS}}}{A_{\mathrm{br}}}(1-\rho(1-f)). \tag{10}$$

In the absolute worst case, a retroreflection sends light exclusively into the instrument field of view so that A_{br} is replaced by the area of the field of view of OCO-2. The ray trace model indicates that we are near this worst case, so that a 2×10^{-4} increase in flux in the sphere (and hence increase in the monitor detector signal of the same order) would yield a $\sim$1% increase in the radiance observed by OCO-2. The fact that the OCO-2 FOV overlaps about 10% of the area of the monitor FOV does not significantly affect this estimate. This bias was not known at the time the preflight calibration coefficients were calculated, and no offsets of this magnitude have been discernable during inflight calibration.

The uncovering of this bias leads to the recommendation that in the calibration of radiometric instruments by integrating spheres, care should be taken to match the viewing area of the monitors to the viewing area of the instrument to be tested. Note that this would give increased robustness against all the sources of inhomogeneity in sphere radiance.

Finally, we note that data were taken to measure potential sphere nonuniformity while the sphere was at NIST in January 2011. An attempt to apply corrections based on this nonuniformity was found to increase the variance of the signal ratio tests, indicating that the corrections decrease the calibration quality. Nonuniformity measurements were taken at two light levels at 100 different locations across the sphere opening. We conclude that two levels alone are insufficient to apply corrections across the entire scale. With all lamps ON, the difference between the radiance in the ASD2 field of view and the OCO-2 field of view was measured to be $<0.05\%$ for the ABO2, 0.3% for the WCO2, and 0.6% for the SCO2, indicating that this has a small effect on the overall scale.

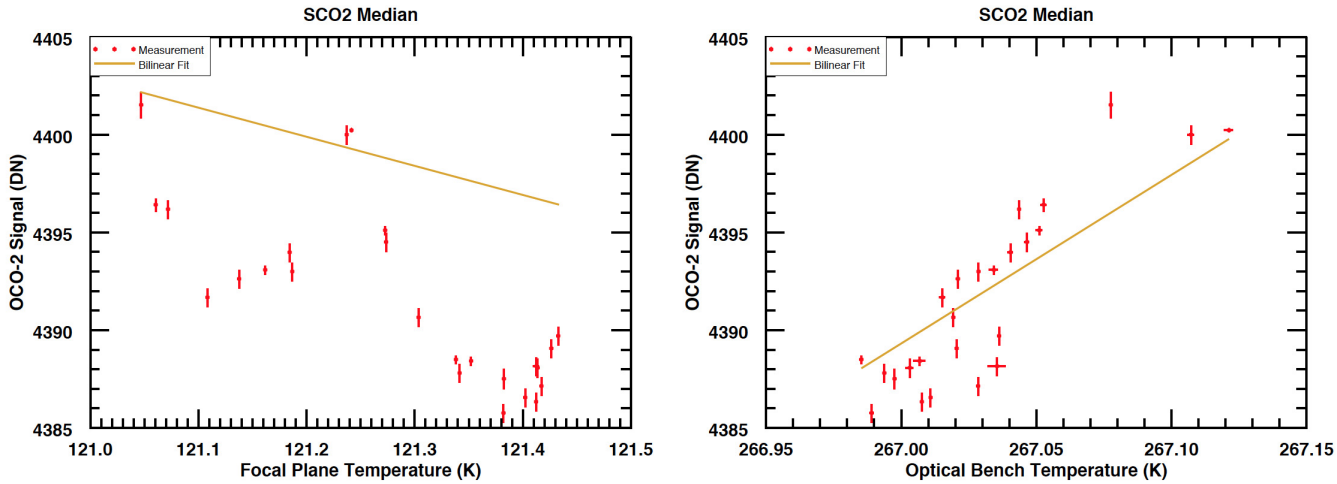

Fig. 9. SCO2 signal is correlated most strongly with the optical bench temperature. The measurement with (T_1, T_2) = (121.24, 267.12) K had a much longer duration, and therefore lower uncertainty and higher weight in the bilinear fit.

B. Dark Offset Correction

To characterize instrument response in the absence of incident light, dark scenes were interleaved into the test program at varying intervals, but typically at least a few times each day. For the final analysis, a mean DN value and uncertainty were recorded for 24 separate dark measurements spanning roughly one week where the instrument was maintained in a nearly stable thermal environment.

Sensitivities to changes in the FPA temperature T_1 were small (on the order of 10 DN/K), owing to the low operating temperature of 120 K. The exception is an increased sensitivity of the WCO2 response to focal plane temperature in the proximity of bad pixels. While the flight software removes the worst of these pixels, crosstalk from these bad pixels can lead to a measurable impact on neighboring good pixels, including entire rows.

The optical bench temperature T_2 produces the largest effect in the SCO2 because of 267-K blackbody radiation from the optical bench produces a significant source of illumination in the passband of the SCO2 cold filter. Sensitivities are on the order of 100 DN/K, with the highest values in the center columns of the focal plane where the optical path from the optics to the detector is least obscured. For reference, the typical background noise of the SCO2 detector is ∼8 DN and the requirement on optical bench temperature stability is 0.15 K over the course of one orbit. SCO2 dark signal dependence on focal plane and optical bench temperatures is shown for the median spectral sample in Fig. 9. In the SCO2, the dependence on T_2 dominates but for the other two bands the dependence on T_2 is comparable to that on T_1.

The quality of the dark correction is evaluated by examining the variance of the corrected DN values across different measurements. On OCO-2 [3], the typical Type A measurement uncertainties in each band after correction were 4 DN, 3 DN, and 6 DN, respectively (uncertainty evaluations based on statistical methods for treating data are termed Type A uncertainties [6]). The OCO-2 values are greatly improved due to more regular data collection and, in the case of the ABO2, due to the lower focal plane temperature. Uncorrected, typical values in each band were 0.24 DN, 0.21 DN, and 3.84 DN. After correction, this was reduced to 0.18 DN, 0.13 DN, and 1.18 DN.

C. Linearity Tests

Results from the signal ratio test show very little variation in radiance ratio as a function of intensity. Fig. 10 shows this ratio for all three bands along with a linear fit. The data are reported in aggregate for all the spectral samples of the spectrometer, and the legend reports the variation seen within the fit region. The radiances used are those calculated from the final radiometric gain coefficients. The ABO2, which has the most saturated features, exhibits the most structure. The SCO2 shows the best performance, even with dark lines. The WCO2 contains no deep absorption, which limits the range over which the linearity is challenged. A complementary visualization shows the ratio as a function of wavelength for the ABO2 band (Fig. 11). While there are still discernable spectral features, they are small in magnitude when compared with the requirement. Additionally, there is very good agreement in the radiance ratios among the three spectrometers. Finally, for the transmission screens with the lowest throughput, the OCO-2 aperture was effectively illuminated by a widely spaced array of point sources, thus substantially underfilling the instrument pupil. This made it difficult to compare against the bright scene. In practice, only the 50% and 75% screens were useful for linearity testing.

During our analysis, we also recognized the possibility of using the principle of flux addition to extract linearity measurements [13]. This principle relies on the fact that radiance from multiple sources adds linearly. In the JPL ISS, there is a set of light sources, along with the variable attenuator on Lamp 8, that can be turned ON in a fixed way to yield a repeatable set of source radiances. NIST used this fact to verify the ASD2 manufacturer's claimed linearity of 1% over the range of levels produced by the ISS. We recommend performing a limited reanalysis of OCO-2 calibration data using this framework to validate the solar-based linearity test.

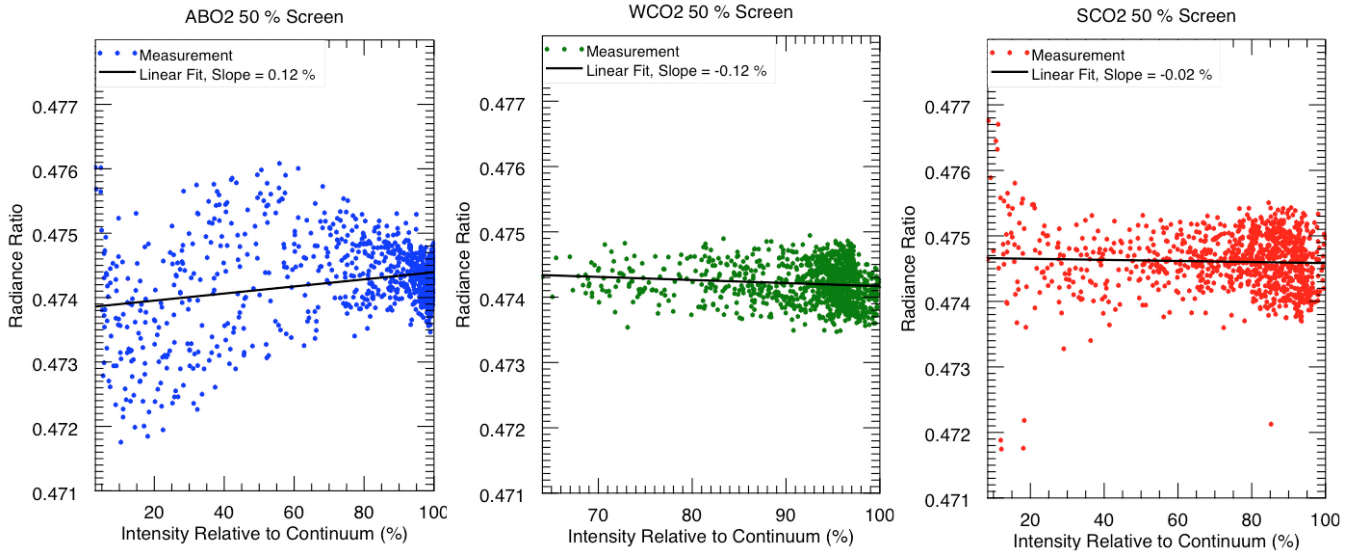

Fig. 10. Ratio of radiances from the open and blocked heliostat is ideally the same for all colors. The slope of a best-fit line of radiance ratio versus normalized intensity was used as a linearity metric.

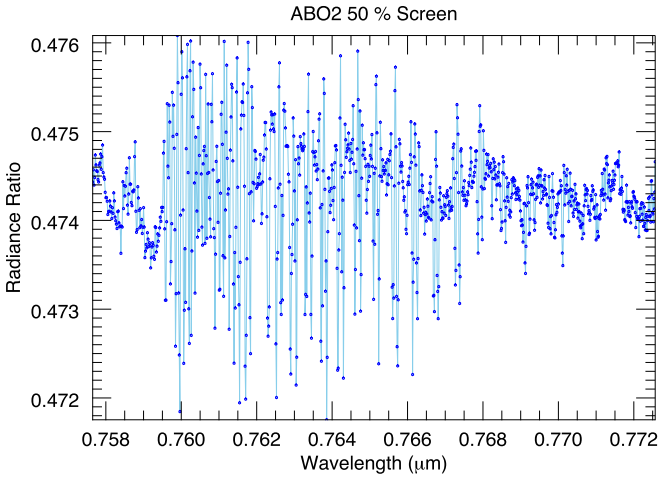

Fig. 11. Molecular spectral band structure is slightly visible in the ABO2 ratios. This is thought to be the results of slight changes in OCO-2's instrument line shape due to the under-filled pupil, not due to linearity errors in the radiometric calibration. This theory is supported by changes in this ratio not being repeatable when the position of the blocking screen changed slightly.

V. Total Calibration Uncertainty

Final radiometric calibration uncertainty can be estimated by inspecting the sources of error in (6) and combining this with the fit uncertainty from (3). In (6), the uncertainty in the assigned radiance of the NPR, the uncertainty in the transfer of the NPR radiance to the ASD2 (which includes both noise and long-term drift in ASD2 responsivity and drift in NPR output), and the nonlinearity of the ASD2 are contributing factors. The uncertainty in the transfer of the NPR radiance to the ASD2 is estimated from the observed variance in the data from dozens of NPR measurements before and after the JPL *in situ* calibrations. Drift and noise in the ASD contribute to the calibration uncertainty, but because the calibration is done for each ISS configuration, nonlinearity of the ASD makes no significant contribution.

A summary of the sources of absolute radiometric uncertainty is given in Table III. The expanded uncertainty, with a coverage factor $k = 2$, is 1.6% for the ABO2 spectrometer, 3.2% for the WCO2 spectrometer, and 2.9% for the SCO2 spectrometer. For normal distributions and $k = 2$, the level of confidence is 95.45% [6]. Additional possible sources of bias are the retroreflection discussed earlier, which could have an effect as large as 1%, and nonuniformity in sphere illumination that leads to a different radiance observed by the ASD2 versus the OCO-2. Together, all the sources of bias and uncertainty are all well within the 5% ($k = 1$) mission requirement.

VI. Applicability to Nonsteady-State Conditions

The calibration procedure described in Section III involved testing the OCO-2 instrument under steady-state or quasi-steady-state illumination. On OCO-2, such testing by itself proved insufficient to fully characterize the radiometric performance of the instrument [3]. This was because during instrument-level testing, the ABO2 and WCO2 FPAs exhibited residual images of sufficient magnitude to preclude meeting mission objectives if uncharacterized and uncorrected. In particular, the ABO2 FPA exhibited an offset proportional to the change in the second derivative of the spectrum over time [14]. This error would decay with a time constant of several seconds. The WCO2 FPA, on the other hand, exhibited a broadband change in the detector offset that was proportional to the mean charge on the detector over the preceding several seconds. Additional tests employing nonsteady-state illumination were therefore performed, and residual image correction algorithms devised and tested, to complete the radiometric calibration of the instrument.

On OCO-2, these problems could not be completely characterized prior to TVAC testing. OCO-2 detectors are of the same make, model, and format as those used for OCO-2, they were originally delivered as flight spares. Therefore, for OCO-2, a more extensive part screening effort was undertaken

TABLE III
UNCERTAINTIES

Uncertainty Source	Measurement Band			Coverage Factor	Uncertainty Type	Method
	ABO2	WCO2	SCO2			
FASCAL Transfer Uncertainty	0.7 %	1.2 %	1.2 %	2	A & B Combined	Stated FASCAL uncertainty
ASD2/NIST ISS (NPR) Repeatability	0.6 %	1.9 %	1.7 %	2	A	Based on long-term observation program in NIST Remote Sensing Laboratory
ASD2 Nonlinearity	1.0 %	1.0 %	1.0 %	2	B	Stated manufacturer nonlinearity
Net Uncertainty of ASD2	**1.4 %**	**2.5 %**	**2.3 %**	**2**	**A & B Combined**	**RSS**
Fit Uncertainty	0.5 %	0.5 %	0.6 %	2	B	Inspection of fit residuals
Erroneous Retro-Reflector Correction	0.1 %	0.2 %	0.2 %	1	B	Based on reflectivity and port fraction
ASD Drift	0.6 %	1.9 %	1.7 %	2	A & B Combined	Assumed to be comparable to NIST
Final Uncertainty	**1.6 %**	**3.2 %**	**2.9 %**	**2**	**A & B Combined**	**RSS of fit residuals, ASD2 uncertainty**

The first three lines contribute to the net uncertainty of the ASD2. The root sum square (RSS) of the next four lines, in bold, is taken to give the final uncertainty.

with a goal of better simulating the scene variability expected during flight. In the course of this screening, we discovered that for the ABO2 detectors, the magnitude of the residual image effect is strongly temperature dependent and that by reducing the operating temperature from 180 to 120 K, the problem could be nearly eliminated. Reducing the temperature to 100 K yielded further improvement, but since the OCO-2 radiators were not large enough to reject that much heat from the cryocooler 120 K was selected as the nominal operational set-point temperature. For the WCO2 and SCO2, part-level screening allowed FPAs with excessive residual image to be rejected. The WCO2 detector that was selected exhibited $<10\%$ of the residual image of its counterpart from OCO-2.

While small residual image behavior was still visible in the selected FPAs, no correction algorithm was implemented for OCO-2. All bands meet the requirement that 1 s after incident radiance changes by half of the dynamic range (Table I), residual image errors are less than instrument noise. Additionally, optical aberrations were designed into the OCO-2 telescope so that consecutive soundings for a given footprint will partially sample the same spatial information. The optical dynamic effects resulting from this are expected to be large compared with the electronic residual image described earlier.

VII. CONCLUSION

Several TVAC tests were performed preflight to fully capture the radiometric performance of the OCO-2 imaging spectrometers. Gain coefficients were calculated for each spectral sample of the instrument by illuminating the spectrometers with a custom integrating sphere at several well-characterized configurations. The instrument's response to light can be characterized by a cubic polynomial. The constant term in this cubic polynomial can be set to zero, because the dark response and its dependence on temperature were characterized and corrected before determining the other coefficients. The end-to-end error budget of each spectrometer was evaluated as a whole, based on the distribution of residuals combining spectral samples, sphere configurations, and test runs. Intermediate transfers from NIST standard sources to the JPL monitor spectroradiometer provided the largest uncertainty. These tests showed that all three spectrometer channels had margin against the 5% absolute performance requirement. The instrument also met requirements on linearity, based on blocking a diffuse solar beam with multiple partially opaque metal screens. The reduction in radiance was both consistent and uncorrelated with intensity, and this test served as the external validation of the parameters calculated using integrating sphere data.

The new integrating sphere, the *in situ* calibration with NIST instruments, the data processing flow that connected ASD data to the transfer standards, and improved part-level screening of FPAs were all improvements for OCO-2 compared with the original OCO-2 instrument. The collaboration with NIST led to a better understanding of the use of internal monitor detectors, in particular, matching fields of view for the monitor detector and the flight instrument was found to be especially important. As part of the characterizations necessary for the ASD2, it was recognized that the JPL ISS could be used to determine the linearity of the ASD2. We predict this approach would lead to the modifications of the ISS that would yield a better ability to measure linearity, relaxing the necessity of independently calibrating each sphere configuration (in principle, only one level would require external calibration), and could remove the dependence of the calibration on the linearity of a transfer radiometer. Early evaluation of the preflight calibration has been conducted using postlaunch data and shows very good agreement. These results will be discussed in a future publication.

APPENDIX

The erroneous adjustment for retroreflection was calculated for each sphere configuration. The retroreflected light not

measured by the monitor was approximated as the difference between the first bounce and the second bounce light. This depends on the reflectivity and port fraction according to

$$\frac{\Delta L_{\mathrm{OCO-2}}}{\Delta L_{\mathrm{MON}}} = 1 + \frac{DN_{\mathrm{ISS}}^{\mathrm{ASD}}(t_5, c)}{DN_{\mathrm{ISS}}^{\mathrm{ASD}}(t_2, c)}(\rho(1-f) - \rho^2(1-f)^2). \tag{11}$$

This model is insufficient, in that it treats the power in a single ray. A more complete model would consider a distribution of rays scattering at a range of angles, then reflected from a larger area. The fractional factors applied were 3%, 7%, and 10% for each band, multiplied by the 1%, 2%, and 2% changes in ASD raw signal for each band. When inserted into (6), the adjustments applied were 0.1%, 0.2%, and 0.2%. Negligible changes to nonlinearity resulted from the ASD ratios varying slightly by configuration, and from incorporating the uncertainty on this adjustment into each measurement.

ACKNOWLEDGMENT

A portion of the research described in this paper was carried out at JPL, California Institute of Technology, under a contract with NASA. Support was also provided by the NIST Greenhouse Gas and Climate Science Measurements program.

REFERENCES

[1] D. Crisp, C. E. Miller, and P. L. DeCola, "NASA Orbiting Carbon Observatory: Measuring the column averaged carbon dioxide mole fraction from space," *J. Appl. Remote Sens.*, vol. 2, no. 1, p. 023508, Mar. 2008.

[2] R. R. Basilio, T. R. Livermore, Y. J. Shen, and H. R. Pollock, "The quest for an OCO (Orbiting Carbon Observatory) re-flight," *Proc. SPIE*, vol. 7827, p. 78270A, Oct. 2010.

[3] C. W. O'Dell *et al.*, "Preflight radiometric calibration of the orbiting carbon observatory," *IEEE Trans. Geosci. Remote Sens.*, vol. 49, no. 6, pp. 2438–2447, Jun. 2011.

[4] B. J. Connor, H. Boesch, G. Toon, B. Sen, C. Miller, and D. Crisp, "Orbiting carbon observatory: Inverse method and prospective error analysis," *J. Geophys. Res.*, vol. 113, no. D5, p. D05305, 2008.

[5] A. Eldering *et al.* (2015). *Orbiting Carbon Observatory (OCO)—2 Level 1B Theoretical Basis Document*. [Online]. Available: http://disc.sci.gsfc.nasa.gov/OCO-2/documentation/oco-2-v7/OCO2_L1B_ATBD.V7.pdf

[6] (2008). *Evaluation of Measurement Data—Guide to the Expression of Uncertainty in Measurement JCGM 100:201X CD*. [Online]. Available: http://www.bipm.org/utils/common/documents/jcgm/JCGM_100_2008_E.pdf

[7] J. O. Day *et al.*, "Preflight spectral calibration of the orbiting carbon observatory," *IEEE Trans. Geosci. Remote Sens.*, vol. 49, no. 7, pp. 2793–2801, Jul. 2011.

[8] C. Frankenberg *et al.*, "The Orbiting Carbon Observatory (OCO-2): Spectrometer performance evaluation using pre-launch direct sun measurements," *Atmos. Meas. Techn.*, vol. 8, no. 1, pp. 301–313, 2015.

[9] R. E. Haring, R. Pollock, B. M. Sutin, R. Blakley, L. M. Scherr, and D. Crisp, "Fabrication and assembly integration of the Orbiting Carbon Observatory instrument," *Proc. SPIE*, vol. 7082, p. 708213, Sep. 2008.

[10] A. Kuze *et al.*, "Vicarious calibration of the GOSAT sensors using the railroad valley desert playa," *IEEE Trans. Geosci. Remote Sens.*, vol. 49, no. 5, pp. 1781–1795, May 2011.

[11] S. W. Brown and B. C. Johnson, "Development of a portable integrating sphere source for the Earth Observing System's calibration validation programme," *Int. J. Remote Sens.*, vol. 24, no. 2, pp. 215–224, 2003.

[12] L. S. Rothman *et al.*, "The *HITRAN* 2008 molecular spectroscopic database," *J. Quant. Spectrosc. Radiat. Transf.*, vol. 110, nos. 9–10, pp. 533–572, 2009.

[13] D. R. White, M. T. Clarkson, P. Saunders, and H. W. Yoon, "A general technique for calibrating indicating instruments," *Metrologia*, vol. 45, no. 2, p. 199, 2008.

[14] D. M. O'Brien, R. Pollock, I. Polonsky, and M. Rogers, "Identification and correction of residual image in the O_2 A-band of the Orbiting Carbon Observatory," *IEEE Trans. Geosci. Remote Sens.*, vol. 49, no. 6, pp. 2426–2437, Jun. 2011.

Robert Rosenberg received the B.S. degree in applied physics from the California Institute of Technology, Pasadena, CA, USA, in 2011. His thesis explored the surface chemistry of photoelectrochemical devices for solar energy conversion. From 2009 to 2011, he was an undergraduate researcher analyzing OCO preflight test data. Since 2011, he has been a Data Scientist with the Jet Propulsion Laboratory, California Institute of Technology. He is a member of the OCO-2 & OCO-3 Calibration Teams and the Center for Infrared Sensors.

Stephen Maxwell received the A.B. degree in physics from the Amherst College, Amherst, MA, USA, in 2000, where he worked on spectroscopic measurements in support of tests of fundamental symmetries, and the M.A. and Ph.D. degrees from Harvard University, Cambridge, MA, USA, in 2003 and 2007, respectively. He received a National Science Foundation Graduate Research Fellowship while in the Physics Department, Harvard University, where he studied the behavior of atoms and molecules at temperatures near absolute zero.

From 2007 to 2010, he was a National Research Council Graduate Research Associate with the National Institute of Standards and Technology (NIST), Gaithersburg, MD, USA, where he continued his research on cold atoms through both experiments and theoretical calculations. In 2010, he joined the Sensor Science Division, NIST. His current research interests include radiometric calibration, environmental remote sensing, and greenhouse gas detection.

B. Carol Johnson received the B.S. degree in engineering physics from the University of Colorado Boulder, Boulder, CO, USA, in 1979, and the M.A. and Ph.D. degrees in astronomy from Harvard University, Boston, MA, USA, in 1980 and 1985, respectively.

Since 1985, she has been a Physicist with the National Institute of Standards and Technology (NIST), Gaithersburg, MD, USA. She held a National Research Council Post-Doctoral Fellowship at the National Bureau of Standards from 1985 to 1987. She supports the Cal/Val Program for the Marine Optical Buoy through collaborations with National Oceanic and Atmospheric Administration, Washington, DC, USA, and the National Aeronautics and Space Administration, Washington, DC, USA, and has designed and built several radiometric artifacts specific for ocean color research. Her current research interests include the development of methods for improved radiometric characterization and calibration of instruments, the transfer of this knowledge to the user community, and improving the metrology of radiometry in remote sensing global climate change research.

Dr. Johnson was a Pickering Fellow and an Amelia Earhart Fellow at Harvard University. She was a recipient of the Arthur S. Flemming award and the U.S. Department of Commerce Bronze, Silver, and Gold awards.

Lars Chapsky, photograph and biography not available at the time of publication.

Richard A. M. Lee, photograph and biography not available at the time of publication.

Randy Pollock received the B.S. degree in engineering and applied science from the California Institute of Technology, Pasadena, CA, USA, in 1991.

He is currently an Instrument Architect with the Orbiting Carbon Observatory 2, Jet Propulsion Laboratory, National Aeronautics and Space Administration, Pasadena, CA.